Computers in Biology and Medicine 112 (2019) 103361

Contents lists available at ScienceDirect

Computers in Biology and Medicine

journal homepage: www.elsevier.com/locate/compbiomed

Optimal route planning for image-guided EBUS bronchoscopy

Xiaonan Zang[a,c], Jason D. Gibbs[a,d], Ronnarit Cheirsilp[a,e], Patrick D. Byrnes[a], Jennifer Toth[b], Rebecca Bascom[b], William E. Higgins[a,*]

[a] School of Electrical Engineering and Computer Science, USA
[b] Department of Medicine, Division of Pulmonary, Allergy, and Critical Care Penn State University, University Park and Hershey, PA, USA
[c] EDDA Technologies, Princeton, NJ, 08540, USA
[d] X-Nav Technologies, Lansdale, PA, 19446, USA
[e] Broncus Medical, San Jose, CA, USA

ARTICLE INFO

Keywords:
Bronchoscopy
Lung cancer
Endobronchial ultrasound
Image-guided surgery systems
Chest CT imaging
Procedure planning

ABSTRACT

The staging of the central-chest lymph nodes is a major lung-cancer management procedure. To perform a staging procedure, the physician first uses a patient's 3D X-ray computed-tomography (CT) chest scan to interactively plan airway routes leading to selected target lymph nodes. Next, using an integrated EBUS bronchoscope (EBUS = endobronchial ultrasound), the physician uses videobronchoscopy to navigate through the airways toward a target node's general vicinity and then invokes EBUS to localize the node for biopsy. Unfortunately, during the procedure, the physician has difficulty in translating the preplanned airway routes into safe, effective biopsy sites. We propose an automatic route-planning method for EBUS bronchoscopy that gives optimal localization of safe, effective nodal biopsy sites. To run the method, a 3D chest model is first computed from a patient's chest CT scan. Next, an optimization method derives feasible airway routes that enables maximal tissue sampling of target lymph nodes while safely avoiding major blood vessels. In a lung-cancer patient study entailing 31 nodes (long axis range: [9.0 mm, 44.5 mm]), 25/31 nodes yielded safe airway routes having an optimal tissue sample size = 8.4 mm (range: [1.0 mm, 18.6 mm]) and sample adequacy = 0.42 (range: [0.05, 0.93]). Quantitative results indicate that the method potentially enables successful biopsies in essentially 100% of selected lymph nodes versus the 70–94% success rate of other approaches. The method also potentially facilitates adequate tissue biopsies for nearly 100% of selected nodes, as opposed to the 55–77% tissue adequacy rates of standard methods. The remaining nodes did not yield a safe route within the preset safety-margin constraints, with 3 nodes never yielding a route even under the most lenient safety-margin conditions. Thus, the method not only helps determine effective airway routes and expected sample quality for nodal biopsy, but it also helps point out situations where biopsy may not be advisable. We also demonstrate the methodology in an image-guided EBUS bronchoscopy system, used successfully in live lung-cancer patient studies. During a live procedure, the method provides dynamic real-time sample size visualization in an enhanced virtual bronchoscopy viewer. In this way, the physician vividly sees the most promising biopsy sites along the airway walls as the bronchoscope moves through the airways.

1. Introduction

Lung cancer has long been the most prevalent form of cancer [1]. A major lung-cancer management procedure entails the staging of the central-chest lymph nodes [2]. This involves two steps. First, the physician uses the patient's 3D X-ray computed-tomography (CT) chest scan and, possibly, a positron emission tomography (PET) scan to select nodes of interest and plan the staging procedure. Next, in the surgical suite, the physician performs the staging procedure to biopsy each node for a tissue sample. Per state-of-the-art practice, biopsies are collected via transbronchial needle aspiration (TBNA) using a minimally invasive EBUS bronchoscope (EBUS = endobronchial ultrasound) [3,4].

An EBUS bronchoscope integrates standard videobronchoscopy and a convex-probe EBUS into a single device. The videobronchoscope gives video of the airway-tree's endobronchial structure, while complementary EBUS gives fan-beam-shaped 2D cross-sectional images of the anatomy extraluminal to the airways at airway-wall locations probed by the EBUS [4–6]. For a particular node, the physician first uses videobronchoscopy to *navigate* the device near the node's general vicinity (within 2–3 cm) and then invokes EBUS to *localize* the node and

---

[*] Corresponding author.
E-mail address: weh2@psu.edu (W.E. Higgins).

https://doi.org/10.1016/j.compbiomed.2019.103361
Received 8 April 2019; Received in revised form 16 July 2019; Accepted 16 July 2019

select a biopsy site for TBNA.

For each aspirated node, a major goal of EBUS TBNA is to collect an *adequate tissue sample*. Technically, an adequate tissue sample is one that [7–9]: (a) allows for a specific disease diagnosis (e.g., malignant cancer, sarcoidosis); or (b) gives sufficient nodal tissue (lymphocytes) to assert that the biopsy needle hits the node. While expert physicians have a success rate approaching 90% via EBUS TBNA for hitting a given node and collecting an adequate tissue sample (assuming multiple passes at a node), it is well known that physicians vary considerably in their ability to localize lymph nodes using EBUS [10,11]. To this point, studies have shown success rates for single passes as low as 55% [7,12,13].

The primary method physicians use for selecting candidate lymph nodes and biopsy sites entails interactively scrolling through the 2D sections of a patient's 3D chest CT scan [3]. As an alternative CT-based *virtual bronchoscopy* (VB), which produces simulated endoluminal airway views resembling bronchoscopic video, enables improved biopsy-site selection [12–14]. On a related front, VB has motivated the recent introduction of image-guided bronchoscopy systems. Such systems have proven to reduce the long-known physician skill differences for bronchoscopic navigation through the airway tree [15–18]. To deploy such a system, *airway routes* leading to the clinical sites of interest are preplanned using the patient's chest CT scan. Next, during the live procedure, the guidance system draws upon the procedure plan and CT-based VB to help the physician navigate the “real” videobronchoscope to each preplanned site [17–22].

Note that lymph nodes lie behind the airway walls, hidden from the bronchoscope's field of view. Also, they can be occluded by large vessels, such as the aorta and pulmonary artery (PA), which act as obstacles. This blindness adds uncertainty to biopsy-needle positioning and significantly accounts for false negative biopsies, inadvertent vessel puncture, and bias toward sampling fewer nodes in the left lung (where much of the major vasculature arises) [9,12,14]. EBUS does provide extraluminal views for selecting biopsy sites, but this entails trial-and-error selection based on 2D views of a complex 3D situation. Thus, while the physician knows a target node's general vicinity, translating this knowledge into a safe entry point while also obtaining the largest possible tissue sample is difficult.

A few preliminary efforts have suggested extending image-based guidance to EBUS [23–25]. These works, however, either required significant interactive image analysis, only provided rudimentary visualization aids for target sites, or were not tailored to EBUS TBNA of the central-chest lymph nodes. Also, none provide the information needed for localizing maximal, safe biopsy sites. In particular, VB-based systems do not indicate the locations of biopsy sites giving maximal biopsy tissue samples, nor do they necessarily indicate the presence of occluding vessels, which hinder safe biopsy. As a result, physicians still routinely turn to interactive CT inspection to decide on biopsy sites.

We propose a route-planning method for optimal localization of safe biopsy sites for EBUS TBNA and demonstrate the method's utility in an image-guided EBUS bronchoscopy system. During procedure planning, the method draws upon a patient's 3D chest CT scan to derive optimal airway routes and associated final poses that indicate biopsy sites giving maximum tissue sampling of each target lymph node via EBUS TBNA. To avoid adverse events arising from major-vessel puncture, the optimal pose abides by a prescribed safety margin away from major vasculature. During the staging procedure, the method provides a dynamic real-time display that highlights safe nodal biopsy sites enabling maximal tissue sampling along with the locations of nearby major vasculature. Using this guidance mechanism, the physician readily visualizes effective biopsy sites as he/she navigates toward a node.

Section II describes our methods and discusses implementation considerations. Section III next demonstrates method performance using data derived from lung-cancer patients. It also illustrates method utility during live image-guided EBUS bronchoscopy. Finally, Section IV offers concluding remarks.

2. Methods

Following the international standard usage of EBUS bronchoscopy for central-chest lymph-node staging, our broad aim is to facilitate successful EBUS TBNA of selected nodes [3–5]. In particular, for each target lymph node $\mathbf{R}_L$, our goal is to find the optimal airway route $\mathbf{r}_o$ that enables safe maximal tissue biopsy during EBUS TBNA.

Two main processing steps occur for deriving optimal routes. First, a 3D chest model, which provides essential anatomical and quantitative information, is computed, based on a patient's preoperative chest CT scan. This is then followed by optimal route planning. Sections II-A through II-C give the details.

2.1. 3D chest model

The 3D chest model consists of the following components:

1) Segmented airway-tree lumen [26].
2) Airway endoluminal surfaces and an airway-surface likelihood image. The airway-surface likelihood image is a simple distance map, whereby the 0-valued isosurface denotes the airway walls (endoluminal surfaces), negative values indicate points within the airway lumen, and positive values refer to points outside the airway tree [27].
3) Airway centerlines, along with associated cross-sectional diameters and branch angles at discrete view sites along each centerline [22,28].
4) Vessel segmentations and surfaces for the major central-chest vessels [29,30]. For lymph-node staging, we segment the aorta, PA, superior vena cava, and azygos vein.
5) Target lymph nodes of interest [31,32].

All components are computed using fully automatic methods validated previously in numerous patient studies, with the exception of the lymph nodes which are semi-automatically defined using the 3D live wire or related tools [22,26–32]. Various figures to follow illustrate many of these components.

2.2. Route planning: mathematical formulation

Section II-B first describes the mathematical basis of our route planning method, while Section II-C outlines the numerical implementation.

For each target node $\mathbf{R}_L$, we derive the optimal route $\mathbf{r}_o$, conditioned on the use of an EBUS bronchoscope. The computation draws upon the 3D chest model and EBUS bronchoscope's physical specifications. Route $\mathbf{r}_o$ starts in the trachea and roughly follows the airway tree's centerline structure. It consists of a connected sequence of device poses

$$\mathbf{r}_o = \{\mathbf{p}_1, \mathbf{p}_2, \mathbf{p}_3, \ldots, \mathbf{p}_o\}, \quad (1)$$

where $\mathbf{p}_1$ is the initial pose in the trachea, poses $\mathbf{p}_2, \mathbf{p}_3, \ldots,$ denote subsequent device positions, and final pose $\mathbf{p}_o$ signifies the biopsy site for collecting the maximum tissue sample possible for $\mathbf{R}_L$ via needle biopsy.

We assume the physician uses the Olympus BF-UC180F linear EBUS bronchoscope (6.9-mm distal-end diameter; 10-MHz transducer), the standard integrated device used by physicians world-wide for EBUS-TBNA lymph-node staging (Fig. 1(a)) [3–6,8,10,11]. Three sets of parameters pertinent to device navigation and biopsy specify the device model (Fig. 1(b)):

- bronchoscope specifications

$$\{d_B, l_B, \psi\}, \quad (2)$$

which define the device's physical characteristics, where d_B and l_B denote the diameter and length of the device tip and ψ indicates the tip's

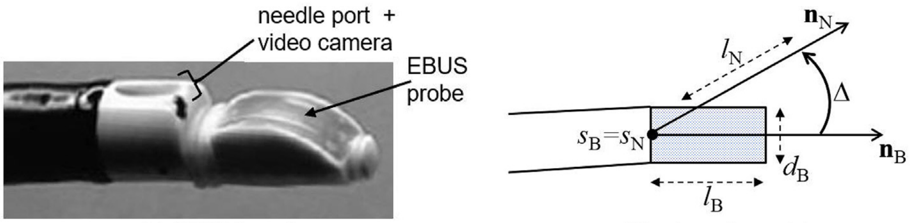

(a) EBUS bronchoscope (b) schematic model

Fig. 1. EBUS bronchoscope. (a) Tip of the Olympus BF-UC180F linear EBUS bronchoscope. (b) Schematic model of the EBUS bronchoscope's tip and extended biopsy needle, with indicated device parameters.

bending angle.

- bronchoscope pose

$$\mathbf{p} = \{\mathbf{s}_B, \mathbf{n}_B, \mathbf{u}_B, \mathbf{r}_B\}, \tag{3}$$

which indicates device location (position and orientation) within the airways. In (3), $\mathbf{s}_B$ signifies the origin of the device tip in global 3D space, while orthonormal vectors $\{\mathbf{n}_B, \mathbf{u}_B, \mathbf{r}_B\}$ form a 3D local coordinate system oriented along $\mathbf{n}_B$, with $\mathbf{n}_B$ indicating the forward direction of the device tip, $\mathbf{u}_B$ indicating the up direction, and $\mathbf{r}_B$ indicating the right direction.

- biopsy needle trajectory

$$\{\mathbf{s}_N, \mathbf{n}_N, l_N\}, \tag{4}$$

which specify the properties of the extended TBNA needle, where $\mathbf{s}_N$ is the needle entry port's origin, vector $\mathbf{n}_N$ indicates the extended needle's direction, l_N equals needle length, and the following conditions apply:

$$\mathbf{s}_N = \mathbf{s}_B, \quad \mathbf{n}_N = \mathbf{n}_B + \Delta\,, \tag{5}$$

where Δ is a fixed offset accounting for the EBUS bronchoscope's needle port configuration.

The optimal route $\mathbf{r}_o$ leading to $\mathbf{R}_\mathrm{L}$ must satisfy four requirements:

a)The device fits within every airway location along route $\mathbf{r}_o$ (6)

b)The device is maneuverable throughout $\mathbf{r}_o$

c) Safe biopsy is possible

d)Final pose p_o enables maximal tissue biopsy of $\mathbf{R}_\mathrm{L}$

The device model (2–5), airway tree and centerlines, target node $\mathbf{R}_\mathrm{L}$, and requirements (6) specify the constraints and search space for the optimization problem.

To derive $\mathbf{r}_o$ as given by (1), we use a depth-first search through the airway tree's centerline structure to construct candidate routes $\mathbf{r}$. As done extensively in our previous work, the centerline structure consists of a hierarchical set of equally-spaced view sites

$$\{\mathbf{v}_1, \mathbf{v}_2, \mathbf{v}_3, \ldots\},$$

with the view sites $\mathbf{v}_i$ constituting the centerlines [22,28,33]. Without loss of generality, let a candidate route $\mathbf{r}$ under construction be given by

$$\mathbf{r} = \{\mathbf{p}_1, \mathbf{p}_2, \mathbf{p}_3, \ldots, \mathbf{p}\}, \tag{7}$$

where $\mathbf{p}$ denotes a candidate pose derived from the view-site set (as discussed in Section II-C, the $\mathbf{p}_i$ are similar to the $\mathbf{v}_i$). Overall, the search moves distally through the airway tree to successive neighboring view sites to identify candidate poses $\mathbf{p}$ and other candidate routes (Section II-C). A candidate pose $\mathbf{p}$ undergoes tests for feasibility and biopsy suitability as discussed next.

For the initial feasibility tests, candidate pose $\mathbf{p}$ must physically enable the physician to maneuver the device toward the node, per requirements (6 ab). More specifically, $\mathbf{p}$ must satisfy the following:

$$d_B < d_A \text{ and } l_B < l_A \tag{8}$$

$$\mathbf{n}_B^T\mathbf{n} \ < \ \cos(\psi) \tag{9}$$

Tests (8–9) were inspired by Gibbs et al., who considered the problem of optimal bronchoscope navigation through the airway tree [22]; we adapt these tests to EBUS bronchoscopy. Eq. (8) requires the device to fit within all airways along a route, where (d_A, l_A) are the minimum airway cross-sectional diameter and segment length encountered along the route. Eq. (9) states a maneuverability constraint, whereby the bronchoscope tip must be able to flex an angle ψ at pose $\mathbf{p}$, where $\mathbf{n}$ indicates the bronchoscope orientation as it looks distally down the airway along the route. If $\mathbf{p}$ fails either test (8–9), then route $\mathbf{r}$ is rejected as a viable route for EBUS TBNA of $\mathbf{R}_\mathrm{L}$ and all successive downstream poses—and constituent airway-tree branches—are eliminated from further consideration. Otherwise, $\mathbf{p}$ undergoes the biopsy-suitability tests.

The biopsy-suitability tests first determine if pose $\mathbf{p}$ permits the TBNA needle to safely pierce node $\mathbf{R}_\mathrm{L}$ and then compute the tissue sample size relative to the device's position at $\mathbf{p}$, when applicable, per requirements (6cd). To ascertain if $\mathbf{p}$ allows the extended needle to pierce $\mathbf{R}_\mathrm{L}$, let $\partial\mathbf{R}_\mathrm{L}$ denote $\mathbf{R}_\mathrm{L}$'s exterior surface boundary. We determine if there exists a nodal surface point $\mathbf{x} \in \partial\mathbf{R}_\mathrm{L}$ satisfying

$$||\mathbf{s}_N - \mathbf{x}||_{\mathbf{n}_\mathrm{N}} \le l_N\,, \tag{10}$$

where $||\mathbf{s}_N - \mathbf{x}||_{\mathbf{n}_\mathrm{N}}$ equals the distance along the extended needle toward $\mathbf{x}$. Two cases arise:

Case 1. If no point $\mathbf{x}$ satisfies (10)—i.e., the needle is not long enough to pierce $\mathbf{R}_\mathrm{L}$ at location $\mathbf{p}$, then three actions occur. First, $\mathbf{p}$ is added to route $\mathbf{r}$. Second, no further calculations take place for $\mathbf{p}$. Third, subsequent successive candidate poses for $\mathbf{r}$ are considered. If no such poses exist—either because they fail feasibility tests (8–9) or a terminating airway endpoint has been reached, then route $\mathbf{r}$ is ruled out from further consideration. Otherwise, successive distinct candidate routes are spawned, which require further construction.

Case 2. If a point $\mathbf{x}$ exists satisfying (10), then the needle is long enough to pierce the node. Thus, $\mathbf{p}$ is a viable biopsy site and, hence, undergoes the subsequent safety test.

To specify the safety test, we point out that while the physician can position the device in many ways locally about a particular route location, they cannot in practice position the device *exactly* at a desired pose. This introduces uncertainty into the needle direction $\mathbf{n}_N$ at pose $\mathbf{p}$. We model this uncertainty via

$$\mathbf{n}_N(\theta, \varphi) = \mathbf{n}_B\cos(\varphi) + \mathbf{u}_B\cos(\theta)\sin(\varphi) + \mathbf{r}_B\sin(\theta)\sin(\varphi) \tag{11}$$

relative to the device's local coordinate system, where θ represents device rotation within the airway and φ is the angle between the needle direction and $\mathbf{n}_B$. In (11), θ and φ are random variables. More specifically, since we have no prior knowledge for the bronchoscope's rotation θ, we assume θ is uniformly distributed over $[0,2\pi]$. Secondly, we assume that the physician tries to cooperate in aligning the biopsy needle along the desired direction $\mathbf{n}_N$, but they will not be able to perform this alignment precisely. To model this, we assume φ decays radially about the desired $\mathbf{n}_N$ over a range $[0, \varphi_{FOV}]$, where $\varphi_{FOV} > 0$ is a parameter. Overall, the uncertainty in needle direction $\mathbf{n}_N(\theta, \varphi)$ occurs over a cone-

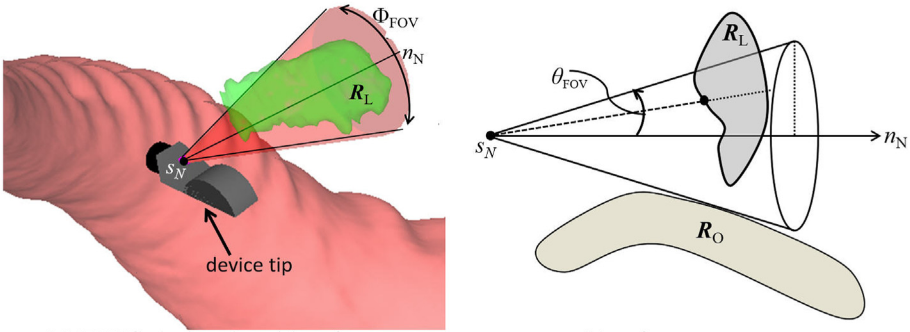

(a) EBUS device tip with safety cone (b) safety cone geometry

Fig. 2. Safety tolerance zone $\Phi(l_S, \varphi_{FOV})$ for a pose per (13). (a) Pictorial view of the EBUS bronchoscope inside an airway with the extended needle passing through a lymph node $\mathbf{R}_{\text{L}}$ (green), and cone-shaped safety tolerance zone. (b) Schematic drawing of a safe pose, where the safety cone about a node $\mathbf{R}_{\text{L}}$ does not intersect a nearby vessel represented by $\mathbf{R}_{\text{O}}$.

shaped field of view (FOV) modeled by joint probability density function

$$p(\theta, \varphi) = \begin{cases} \frac{\varphi_{FOV} - \varphi}{\pi \varphi_{FOV}^2}, & \varphi \in [0, \varphi_{FOV}] \text{ and } \theta \in [0,2\pi] \\ 0, & \text{otherwise} \end{cases} \tag{12}$$

Function $p(\theta, \varphi)$ achieves a maximum when the needle is exactly aligned with the desired $\mathbf{n}_N$ and decays linearly over the cone. Given (12), we now define the safety requirement

$$\Phi(l_S, \varphi_{FOV}) \cap \mathbf{R}_{\text{O}} = \varnothing, \tag{13}$$

where: (1) $\Phi(l_S, \varphi_{FOV})$ denotes a 3D safety tolerance cone of length $l_S > l_N$ and angular width φ_{FOV} oriented at $\mathbf{s}_N$ along direction $\mathbf{n}_N$; and (2) $\mathbf{R}_{\text{O}}$ denotes an obstacle (Fig. 2). If the physician swings the length-l_N needle anywhere inside the cone Φ without piercing any unsafe obstacle-laden zones—i.e, a blood vessel, then the local pose is deemed safe. If pose $\mathbf{p}$ fails (13), it is ruled out from further consideration. Since the safety cone's extent l_S is greater than the extended needle length l_N, an extra buffer zone exists for added safety.

Continuing, define the tissue sample size D as the segment length of the extended biopsy needle piercing $\mathbf{R}_{\text{L}}$'s volume. Tissue sample D of the extended needle specified by (4) is given by

$$D(\mathbf{s}_N, \mathbf{n}_N, l_N) = \int_0^{l_N} \chi(\mathbf{s}_N + l\, \mathbf{n}_N) dl \tag{14}$$

where $\chi(\mathbf{m})$ is an indicator function ($\chi \to \{0,1\}$) stating whether node $\mathbf{R}_{\text{L}}$ is pierced by the needle at location $\mathbf{m}$. Next, to account for device ambiguity during final alignment, the expected tissue sample size Γ_o over all possible needle positions relative to the cone-shaped FOV per (12) is computed:

$$\begin{aligned} \Gamma_o &= E[D(\mathbf{s}_N, \mathbf{n}_N(\theta, \varphi), l_N)] \\ &= \int_0^{\varphi_{FOV}} \int_0^{2\pi} D(\mathbf{s}_N, \mathbf{n}_N(\theta, \varphi), l_N)\, p(\theta, \varphi)\, d\theta d\varphi \end{aligned} \tag{15}$$

where $0 \le E[D(\mathbf{s}_N, \mathbf{n}_N(\theta, \varphi), l_N)] \le l_N$, with larger values reflecting a greater expected tissue sample size.

The search concludes when the route $\mathbf{r}_o$ giving the globally maximum expected tissue sample of target node $\mathbf{R}_{\text{L}}$ is found, as given by

$$\mathbf{r}_o = \arg\left\{ \max_{\mathbf{r} \in \mathbf{S}_f} E_{\mathbf{r}}[D(\mathbf{s}_N, \mathbf{n}_N, l_N)] \right\}, \tag{16}$$

where $\mathbf{S}_f$ denotes the set of feasible routes that enable safe biopsy and $E_{\mathbf{r}}[D(\mathbf{s}_N, \mathbf{n}_N, l_N)]$ is the expected tissue sample for a particular route $\mathbf{r}$. Note, of course, that many poses $\mathbf{p}_i$ along route $\mathbf{r}_o$ could enable a biopsy, but the pose $\mathbf{p}_o$ enabling maximal tissue biopsy Γ_o always terminates $\mathbf{r}_o$.

Tissue sample metric Γ_o establishes a firm quantitative measure based on mathematical optimization. It is very similar to the ad hoc metrics used in the previous nodal sampling studies of Hopper and Bentancourt [12,13]. In particular, both investigators recognized that it is difficult, if not impossible, for a physician to "exactly" hit a selected biopsy site, with Hopper defining a metric based on the notion of hitting the middle 75% of a node's mass and Betancourt employing a metric that considers if a biopsy site admits a tissue sample of any size over multiple needle entry angles. The concept behind these metrics is also in line with the goal of obtaining an *adequate tissue sample* defined in Section I and elaborated on further in the quantitative studies of Section III [7–9].

2.3. *Route planning: implementation*

The calculations required to construct candidate routes $\mathbf{r}$ of the form (7) entail two steps: 1) derive candidate feasible safe poses; and 2) determine the expected tissue sample of each pose. As the central airways relevant to lymph-node staging typically have diameters >9.0 mm (trachea → subsegmental airways), we use patient chest CT scans having voxel dimensions $(\Delta x, \Delta y, \Delta z) < 1.0$ mm; such scans provide more than adequate airway endoluminal surfaces for the calculations [22].

Without loss of generality, let $\mathbf{v}$ denote the next view site to consider along the airway centerline being followed by route $\mathbf{r}$. Many possibilities exist for candidate poses $\{\mathbf{p}_{i,j}\}$ at $\mathbf{v}$. As shown in Fig. 3(a), we chose candidate pose locations

$$\mathbf{s}_B^i, \ i = 1,2, \ldots$$

as 3D voxel locations in the adjacent airway-lumen plane perpendicular to $\mathbf{v}$. The airway-tree segmentation is subsampled to limit the number of pose locations considered. Now, at a given location $\mathbf{s}_B^i$, certain subvolumes of target node $\mathbf{R}_{\text{L}}$ could enable better device accessibility and/or biopsy than others. Therefore, multiple forward directions $\mathbf{n}_B^{ij}$ with corresponding needle directions

$$\mathbf{n}_N^{ij}, \ j = 1,2, \ldots, J$$

are derived for each $\mathbf{s}_B^i$, where $\mathbf{n}_N^{ij}$ points toward the centroid of the j^{th} subvolume constituting $\mathbf{R}_{\text{L}}$ (Fig. 3(b)). We define a subvolume as a connected cluster of voxels constituting $\mathbf{R}_{\text{L}}$, where clusters are found by modified k-means clustering ($J = 25$ in our implementation) [34]. This gives candidate poses

$$\mathbf{p}_{ij} = \{\mathbf{s}_B^i, \ \mathbf{n}_B^{ij}, \ \mathbf{u}_B^{ij}, \ \mathbf{r}_B^{ij}\}$$

with needle poses $\mathbf{n}_N^{ij}$, where $\mathbf{s}_N^i = \mathbf{s}_B^i$ and $\mathbf{n}_N^{ij} = \mathbf{n}_B^{ij} + \Delta\mathbf{n}$ per (5). Vectors $\mathbf{u}_B^{ij}$ and $\mathbf{r}_B^{ij}$ can be arbitrary, provided they form an orthonormal basis relative to $\mathbf{n}_B^{ij}$.

Poses $\mathbf{p}_{ij}$ passing feasibility tests (8–9) are retained for further route construction. To test (8–9), we model the device tip as a discrete cylinder made up of circular cross-sections spaced a distance

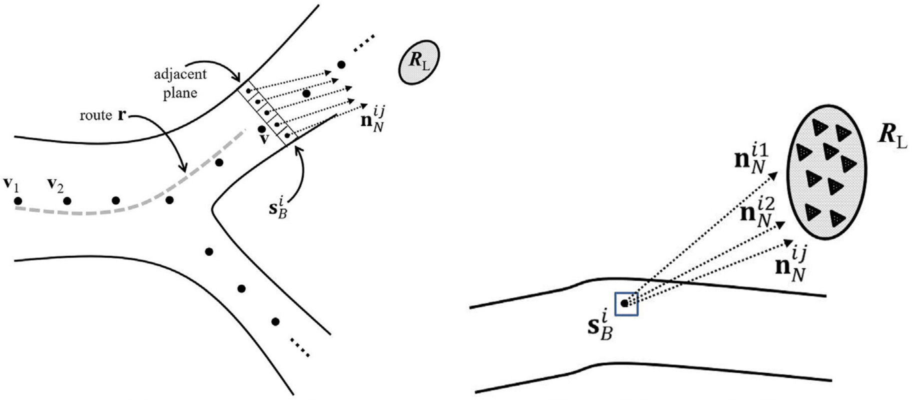

(a) route computation (b) candidate needle directions

Fig. 3. Schematic depiction of optimal route computation. (a) Search for new potential pose locations $\mathbf{s}_B^i$, $i = 1,2, ...,$ and needle directions $\mathbf{n}_N^{ij}$, $j = 1,2, ...,J$ for route $\mathbf{r}$ (dotted line) under construction; "•" points indicate view sites constituting the precomputed airway centerlines, with $\mathbf{v}$ indicating the current view site under consideration. (b) Multiple needle directions $\mathbf{n}_N^{ij}$ found for a given pose location $\mathbf{s}_B^i$; triangles inside lymph node $\mathbf{R}_\mathrm{L}$ indicate the j^{th} subvolume of $\mathbf{R}_\mathrm{L}$.

$\min(\Delta x, \Delta y, \Delta z)$ apart, and determine if any cross-section hits the airway-surface likelihood image's 0-valued isosurface. Computations based on the likelihood image are far simpler than using airway-tree surface polygonal mesh.

Feasible poses that result in the needle piercing the node (test (10)) and that are also safe (test (13)) undergo expected tissue sample size calculation. To compute a pose's expected tissue sample, note that $\mathbf{R}_\mathrm{L}$ is not a function per se, but instead is a connected set of voxels in the CT scan. Thus, the line integral (14) for $D(\cdot, \cdot, l_N)$ and the expected sample size relation (15) cannot be directly evaluated. Therefore, we compute $D(\cdot, \cdot, l_N)$ for a needle trajectory $\{\mathbf{s}_N, \mathbf{n}_N, l_N\}$ in (14) using the node's polygonal surface. The surface triangles that intersect the needle trajectory as it enters and exits the node are first found. The dot product of the outward-facing normal $\mathbf{t}$ of a surface triangle and the needle direction $\mathbf{n}_N$ disambiguates whether the needle is entering or leaving the surface; i.e., if

$$\mathbf{t}^T \cdot \mathbf{n}_N < 0, \tag{17}$$

then the needle is entering the node; otherwise, it is exiting (Fig. 4). The distance between these triangles relative to $\mathbf{n}_N$ gives $D(\mathbf{s}_N, \mathbf{n}_N, l_N)$. The expected tissue sample size (15) for pose $\mathbf{p}_{ij}$ is then approximated as

$$E\left[D(\mathbf{s}_N^i,\ \mathbf{n}_N^{ij}(\theta, \varphi),\ l_N)\right] \approx \sum_{k=1}^{M} \omega(\theta_k, \varphi_k) \cdot D(\mathbf{s}_N^i,\ \mathbf{n}_N^{ij}(\theta_k, \varphi_k),\ l_N), \tag{18}$$

where $\omega(\theta_k, \varphi_k)$ discretizes pdf $p(\theta, \varphi)$ in (12) at equally spaced angular offsets

$$(\theta_k, \varphi_k), \quad k = 1,2, ...,M \tag{19}$$

within $p(\theta, \varphi)$'s cone-shaped region of support, $\sum_{k=1}^{M} \omega(\theta_k, \varphi_k) = 1$, and needle direction $\mathbf{n}_N^{ij}(\theta_k, \varphi_k)$ is offset from $\mathbf{n}_N^{ij}$ by (θ_k, φ_k) relative to coordinate system $\{\mathbf{n}_B^{ij},\ \mathbf{u}_B^{ij},\ \mathbf{r}_B^{ij}\}$ per (11). Calculations for (10), (13), and (17–18) draw upon the surface polygonal meshes of the node $\mathbf{R}_\mathrm{L}$ and obstacles $\mathbf{R}_\mathrm{O}$ and are computed efficiently using the GPU's specialized hardware acceleration [35].

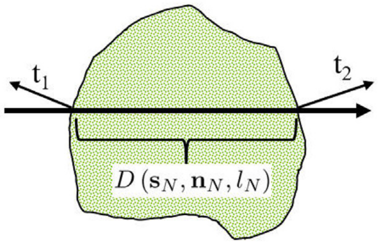

Fig. 4. Calculation of a needle's tissue sample size through a target node. The needle, oriented along direction $\mathbf{n}_N$, pierces a node (green). The outward-facing normal vectors of the two node surface triangles intersected by the needle are $\mathbf{t}_1$ and $\mathbf{t}_2$. $D(\mathbf{s}_N, \mathbf{n}_N, l_N)$ equals the needle's DOS of the node.

To solve optimization problem (16), the search through the airway tree for viable routes continuously updates the route $\mathbf{r}$ whose terminating pose gives the current maximum expected tissue sample size found. At the search's conclusion, optimal route $\mathbf{r}_o$ is obtained. As Section III illustrates, the sample size information vividly portrays effective biopsy sites. It also efficiently translates into intuitive visualization cues during live guidance of EBUS bronchoscopy, with sample size information computed in real-time at all sites visible inside the airway at the bronchoscope's current pose.

3. Results

Section III-A presents quantitative tests of the proposed route-planning method. It also illustrates the potential advantages of the method during procedure planning and live EBUS bronchoscopy. Next, Section III-B demonstrates our method's utility for live procedure guidance in an image-guided bronchoscopy system.

All tests were run on a Dell Precision T5500 PC (64-bit Windows 7, dual 2.8 GHz 6-core CPUs, 24 GB RAM) powered by an nVidia Quadro 4000 2 GB PCIe graphics engine and a Matrox Vio IA/OA frame grabber. We coded all software using C+ + developed in Visual Studio 2012 and drew upon several packages, including Qt, OpenGL, vtk, and the Visualization Library. Some data-intensive operations were parallelized using OpenMP and nVidia's compute-unified device-architecture (CUDA) tools.

3.1. Route-planning tests

We tested the method using 3D chest CT scans obtained under informed consent from 10 lung-cancer patients (age 51–79 years; 6 M: 4F). The scans were produced by various Siemens multi-detector X-ray CT scanners. All scans consisted of a contiguous series of 512×512 2D sections with axial-plane voxel resolution ($\Delta x = \Delta y$) ranging over $[0.5\text{mm},\ 0.9\text{mm}]$ and section thickness $\Delta z = 0.5$ mm.

For each scan, we computed the 3D chest model and segmented target lymph nodes following the procedure of Section II-A. The attending physician, drawing upon the radiologist's CT scan report, chose the target nodes. The best-fitting 3D ellipsoid was then derived for each node, with principal-axis lengths (L_a, L_b, L_c) noted [36]. 31 lymph nodes were selected for the 10 scans (Table 1). The "median [min, max]" number of nodes selected per scan was 3 [1,7].

Per the standard lung-cancer staging clinical guideline, 30/31 lymph nodes had a long axis >10 mm [2,3]. We also note that 20 nodes

Table 1
Characteristics of 31 lymph nodes selected from 10 chest ct scans. "MEAN" and "[min, max]" denote the mean and [minimum, maximum] values of a property over all 31 nodes. Measures are in mm.

property	mean	[min,max]
L_a	16.7	[7.3, 37.0]
L_b	11.5	[5.4, 38.8]
L_c	17.1	[5.3, 44.5]
long axis	20.8	[9.0, 44.5]
short axis	10.1	[5.3, 25.4]

had a long-axis length <20 mm, *shorter* than the extended biopsy needle's length $l_N = 20$ mm. Lastly, 10/31 nodes had a short axis > 10 mm. Based on the standard International Association for the Study of Lung Cancer (IASLC) lymph-node station map, the nodes were located in the following central-chest regional stations [37]: station 4R, 7 nodes; 4L, 4 nodes; 7, 9 nodes; 10L, 4 nodes; 10R, 2 nodes; 11L, 2 nodes; 11R, 3 nodes.

The Olympus BF-UC180F linear EBUS bronchoscope fixes the following parameters for all tests (Fig. 1): 1) bronchoscope insertion-tube diameter $d_B = 6.3$ mm; 2) bronchoscope tip length $l_B = 10$ mm; 3) extended needle length $l_N = 20$ mm; and 4) needle port offset $\Delta = 20°$. Also, we constrained the maximum bronchoscope bending angle to $-65° \le \psi \le +65°$. While the device actually has a feasible range of $-90°$ (down) $\le \psi \le +120°$ (up), we chose ψ conservatively to limit extreme device flexing. Safety cone parameters were set to $\varphi_{FOV} = 20°$ and $l_S = 25$ mm, per (12) and (13). A later parameter-sensitivity test varies φ_{FOV}.

To evaluate the quality of a given lymph node's optimal route $\mathbf{r}_o$ and $\mathbf{r}_o$'s corresponding final pose $\mathbf{p}_o$ signifying the optimal airway-wall biopsy site, we consider the following metrics that measure: (a) if a needle biopsy hits a node; and (b) the size/adequacy of obtainable tissue samples:

1) Optimal tissue sample size

$$\Gamma_o = E[D(\mathbf{s}_N, \mathbf{n}_N(\theta, \varphi), l_N)] \tag{20}$$

per (15).

2) Maximum tissue sample size

$$\Gamma_{\max} = \max_{\theta_k, \varphi_k} D(\mathbf{s}_N^i, \mathbf{n}_N^{ij}(\theta_k, \varphi_k), l_N) \tag{21}$$

per (18–19).

3) Adequacy

$$\alpha = \frac{\Gamma}{l_N} \tag{22}$$

where Γ equals either Γ_o or $\Gamma_{\max}$ from (20–21).

4) Success in hitting a node:
   a) at any needle entry angle
   b) at some but not all entry angles

Metrics Γ_o and $\Gamma_{\max}$ measure absolute tissue sample sizes in mm and range from 0 mm (no tissue sampled) to l_N mm (biopsy needle completely pierces the node). As stated earlier, Γ_o measures the maximum expected tissue sample, given that a physician may not be able to pierce the node at the precise optimal entry angle. $\Gamma_{\max}$, on the other hand, denotes the maximum possible tissue sample obtainable (in the unlikely event) that the physician pierces the node at the optimal needle entry angle within the safety cone φ_{FOV}. Clearly,

$$\Gamma_o \le \Gamma_{\max}.$$

Both Γ_o and $\Gamma_{\max}$ are considered in the adequacy and success measures.

Adequacy α ranges over [0.0, 1.0] and follows the standard definition of an adequate tissue sample. In particular, we use Hong's quantitative A through E grades for sample adequacy [7]: A, high tissue sample size (between 60 and 100% of the needle core gives diagnostic tissue); B, moderate (30–59%); C, low (5–29%); D, scant (<5%); E, none (no lymphocytes). Thus, $\alpha = 1.0$ denotes a 100% biopsy sample size (complete needle core contains diagnostic tissue). Following Hong, an adequate tissue sample must be at least grade C to have sufficient diagnostic cells to enable a specific diagnosis or determine if a target node was indeed sampled. In other words,

$$\alpha \ge 0.05 \quad \rightarrow \quad \text{tissue sample is } \textit{adequate} \tag{23}$$

Adequacy clearly depends on absolute node size, as only large nodes with $\max(L_a, L_b, L_c) > l_N$ can give $\alpha = 1.0$, while smaller nodes with long axis $<l_N$ can never give $\alpha = 1.0$.

The biopsy success measures for hitting a node were suggested by Betancourt with equivalent metrics used by Hopper [12,13]. The metric "Success in hitting a node at any entry angle" is directly analogous to Hopper's "success in sampling the central 75% of a lymph node's mass" measure, while the metric "success at some but not all entry angles" is directly comparable to Hopper's "successful biopsy" measure. Strictly speaking, a selected biopsy site is deemed a "success" if the biopsy needle pierces the node, regardless of the adequacy α of the obtained tissue sample. In practice, for a chosen biopsy site, the "any angle" measure implies that the needle pierces the node's main central bulk; thus, an adequate tissue sample is likely attainable over any needle entry angle. The "some angles" measure implies that an adequate tissue sample is less attainable.

Because lymph nodes always exist outside the airways, the biopsy needle does not sample any tissue for a given node until it pierces the node. As given by constraint (10), the needle travels a distance

$$d_P = ||\mathbf{s}_N - \mathbf{x}||_{\mathbf{n}_N} \tag{24}$$

Before it pierces the node at surface point $\mathbf{x}$. Thus, distance d_P affects tissue sample size, where

$$\Gamma_o, \ \Gamma_{\max} \ \le \ l_N - d_P \ ,$$

As shown in Fig. 5. Clearly, d_P also reduces the potential adequacy α of a biopsy sample.

Table 2 summarizes the metric values attained by the proposed route-planning method over the 31-node test set. Under the given constraints, safe routes did not exist for 6/31 nodes, implying that it is inadvisable to attempt biopsies for these nodes. Therefore, biopsy size/adequacy metrics don't exist for these nodes, and, hence, are excluded in Table 2. For the 25/31 nodes giving safe, feasible routes, the mean values of the absolute sample size metrics were $\Gamma_o = 8.4$ mm and $\Gamma_{\max} = 11.1$ mm. For sample adequacy α in (22), we substituted Γ_o and $\Gamma_{\max}$ to give mean values $\alpha_o = 0.42$ and $\alpha_{\max} = 0.56$, respectively.

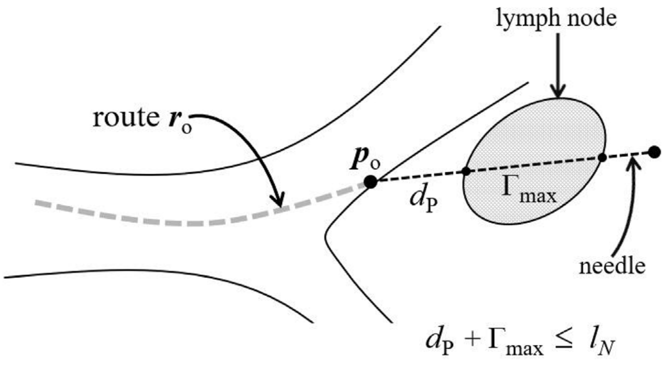

Fig. 5. Geometry for a biopsy needle of length l_N sampling a lymph node at the final pose $\mathbf{p}_o$.

Table 2

Optimal route planning results over 31-node test set. “no.” Denotes the number of selected nodes for each patient. “opt.” Denotes the number of nodes having a feasible optimal airway route $\mathbf{r}_o$. Unitless metrics Γ_o, $\Gamma_{\max}$, and d_P are in mm. Metrics α_o and $\alpha_{\max}$ correspond to the adequacy metric α using Γ_o and $\Gamma_{\max}$, respectively, for Γ in (22). “time” denotes computation time for route planning in sec (3d chest model computation excluded). Most measures are listed as a [min, max] range over all nodes for a given patient. The last two rows give the mean±sd and [min, max] range over all nodes.

Patient	No.	Opt.	Γ_o	$\Gamma_{\max}$	d_P	α_o	$\alpha_{\max}$	Time
1	5	5	[2.5, 10.9]	[3.5, 14.7]	[5.3, 15.8]	[.13, .55]	[.18, .74]	[5.8, 124]
2	3	1	7.1	7.6	12.4	.36	.38	[13, 261]
3	7	7	[1.0, 12.6]	[1.6, 17.2]	[3.3, 18.0]	[.05, .63]	[.08, .86]	[10, 87]
4	4	3	[7.8, 10.3]	[11.9, 15.1]	[4.8, 7.2]	[.39, .52]	[.60, .76]	[5.2, 79]
5	3	1	13.4	18.0	1.6	.67	.95	[2.8, 189]
6	2	2	[3.7, 18.6]	[5.3, 18.8]	[1.8, 14.0]	[.19, .93]	[.27, .94]	[51, 167]
7	2	1	1.5	2.2	17.5	.08	.11	[27,32]
8	1	1	11.2	16.2	4.0	.56	.81	57
9	2	2	[6,9, 14.7]	[9.9, 17.0]	[3.4, 10.4]	[.35, .74]	[.50, .85]	[54, 139]
10	2	2	[11.9, 17.1]	[17.1, 17.9]	[2.5, 2.9]	[.60, .86]	[.86, .90]	[111, 353]
overall	31	25	8.4±4.7	11.1±5.4	8.5±5.2	.42 ± .24	.56 ± .27	77±76
			[1.0, 18.6]	[1.6, 19.0]	[1.6, 18.0]	[.05, .93]	[.08, .94]	[2.8, 353]

Finally, since the proposed method *automatically* selects the optimal biopsy site, which specifies the optimal needle entry angle for maximally sampling a given node, the 25 nodes admitting safe, feasible routes all by definition enable a successful biopsy, implying a 100% success rate in hitting a node. While success only requires α_o, $\alpha_{\max} \geq 0.0$, we note that adequate tissue samples were obtainable in theory for all of these nodes per (23).

We next compare our method to previous central-chest lymph node studies [7,12,13]. As a caveat, we caution that while all studies, including ours, consider lymph nodes within the standard lymph-node staging guidelines, the presented study results are dependent on the choice of nodes and patients. In our work, we did endeavor to consent patients without selection bias.

To begin, Table 3 compares the success in selecting nodal biopsy sites between our method and the two CT-based biopsy-site selection studies of Hopper and Betancourt [12,13]. Both studies considered the same two methods for *manual* interactive selection of lymph-node biopsy sites, which still serve as the clinical standard for lymph-node staging: 1) 2D CT section viewing; and 2) CT-based virtual bronchoscopic endoluminal airway renderings that also depict an extraluminal node's view projected onto the airway wall (e.g., Fig. 8(b)). Hopper's nodal views, however, can be truncated in depth, obscuring their appearance. Note that the test data employed by the three studies are comparable. Hopper drew upon nodes having a mean diameter ≈ 2.0 mm, while Betancourt did not specify node size but evidently followed clinical guidelines.

Table 3 clearly shows our method's superiority in selecting potentially successful biopsy sites. Furthermore, our method has numerous advantages over the existing CT-based approaches. In particular, it is *automatic*— independent of physician skill — and provides optimal sites giving maximal tissue samples; the manual approaches give no indication of possible tissue sample sizes. It also provides needle entry angles and flags unsafe biopsy sites, whereas the manual methods only help select airway wall puncture sites and have no means for indicating potentially hazardous biopsy sites. Finally, as demonstrated later, our method facilitates a dynamic visualization mechanism that helps select multiple biopsy sites during a live staging procedure. Interestingly, the mean distance from the airway wall to the node, d_{p}, was 8.5 mm for our method (Table 2), whereas Hopper indicated a mean d_{p} = 8.8 mm for the VB-based approach (they found a mean d_{p} = 14.1 mm for the inferior 2D CT approach).

Table 3

Comparison of biopsy success results. The “success” column lists the two metrics for biopsy success, with “any angle” and “some angles” referring to the success in hitting a node “at any needle entry angle” and “at some but not all entry angles,” respectively. The two columns corresponding to “hopper” and “betancourt” relate to the hopper and betancourt studies, respectively [12,13]. For each of these studies, “ct” refers to using 2d ct section scrolling to select a nodal biopsy site, while “vb” refers to viewing ct-based virtual bronchoscopic renderings of endoluminal airway structure. The last column pertain to our proposed route-planning method. The numbers indicate the percentage of successful biopsies attainable for a given biopsy site selection method.

	Hopper		Betancourt		
Success	CT	VB	CT	VB	Proposed
any angle	41	70	43	71	100
some angles	55	83	56	94	100

As a second comparison, Table 4 compares the attainable tissue adequacy between our method and the clinical nodal sampling study of Hong [7]. (As in the other studies, Hong considered lymph nodes meeting the standard clinical guideline with a mean short axis = 13.5 mm) Hong reported results for two needle sizes commonly used for collecting nodal tissue samples [9]. For our method, we report potentially attainable tissue adequacy values based on α_o and $\alpha_{\max}$ for each test node in our data set. Table 4 reports on the standard tissue adequacy measure α per (23) along with other adequacy measures over Hong's A-E adequacy grades summarized earlier.

The results clearly indicate that our proposed method, whether α_o or $\alpha_{\max}$ is used, suggests biopsy sites enabling a higher percentage of adequate tissue samples than standard nodal sampling. In addition, our method never suggested inadequate biopsy sites, while the standard approach had ≥ 23% inadequate sites and ≥ 18% outright misses of a node. Table 4 also shows that our method offers better potential performance for a more stringent tissue adequacy measure (grade A or B) — this is important given the ongoing problem of improving overall diagnostic yield, as discussed in Section IV.

As expected, a lymph node's size, shape, and location significantly influence the capacity for allowing a suitable route for TBNA. Biopsy potential is affected by the needle's distance to a node, as specified by d_P in (24) and by a node's proximity to major vasculature. If the node lies

Table 4

Comparison of tissue sample adequacy results. The first two rows give results from the Hong study [7], while the latter two rows refer to our proposed method using the two interpretations of adequacy, α_o and $\alpha_{\max}$, given in Table 2. “a-c”, “a-b”, etc., refer to Hong's quantitative grades for sample adequacy. Note that column “a-c” corresponding to a standard definition (23) of an adequate tissue sample. All measures are a percentage on the [0, 100] scale.

	A-C	A-B	D-E	E only
	$\alpha \geq 0.05$	$\alpha \geq 0.30$	inadequate	none
Hong (21-gauge)	77	60	23	18
Hong (22-gauge)	55	36	45	21
Proposed α_o	100	60	0	0
Proposed $\alpha_{\max}$	100	76	0	0

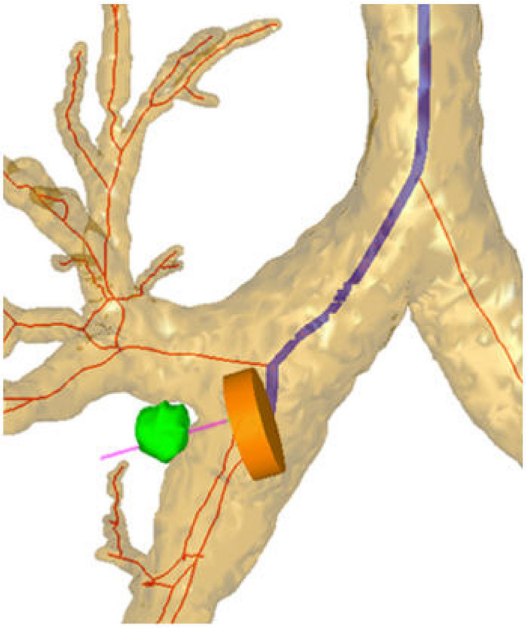

Fig. 6. Small station 11R lymph node of patient 3 that is completely pierced by the needle at optimal pose $\mathbf{p}_o$. The view focuses on the right-middle lung region. In this figure and others to follow, the light brown surface denotes the airway tree, red lines represent precomputed centerlines, the blue line indicates the optimal route $\mathbf{r}_o$ for the target node (green region). Also, the orange cylinder represents the bronchoscope tip position, and the magenta line indicates the needle.

far from an airway, then less of the biopsy needle is available to sample the node. Similarly, if the node is situated near major vessels, then a safety margin must be maintained, restricting the possible poses for sampling the node. Regarding the nodes yielding a feasible route, 10 nodes gave $\Gamma_o > 10$ mm, which all corresponded to larger nodes, while 6 nodes gave $\Gamma_o < 5$ mm implying weaker biopsy potential. In addition, 22/25 lymph nodes having a feasible route exhibited the property

$$\Gamma_{\max} + d_{\mathrm{P}} \approx l_N \ ,$$

implying that after the biopsy needle traverses the gap between the airway wall and nodal surface (given by d_{P}), the remainder of the needle fully pierces the node. This does not, however, necessarily predict a large tissue sample. For example, a station 10R node for patient 3 gave $\Gamma_{\max} + d_{\mathrm{P}} = 19.6$ mm $\approx l_N$ but a weak tissue adequacy $\alpha_o = 0.05$. Conversely, a small 11R node for patient 3 with ($R_a = 6.7$ mm, $R_b = 9.9$ mm, $R_c = 8.5$ mm) gave $d_{\mathrm{P}} + \Gamma_{\max} = 10.9$ mm $< l_N$ and a solid $\alpha_o = 0.29$ (Fig. 6).

As a practical point, no node gave tissue sample sizes Γ equal to the needle length l_N or tissue adequacy $\alpha = 1.0$. Yet, adequacy α clearly alerts the physician to the biopsy potential of selected nodes. Many nodes have very good biopsy potential, while other nodes have poorer potential. The discovery of this reality—before the procedure—is major advantage offered by our method and alerts the physician to make sufficient needle passes.

The 6 lymph nodes not yielding a feasible route were all situated overly closely to a blood vessel, thus failing the safety constraint (13). For example, a station 11L lymph node for patient 5 existed directly anterior to the PA, which excessively reduces the margin for a safe biopsy (Fig. 7). This ability to identify such problematic situations during procedure planning is another significant benefit of our method, as it could help prevent adverse events (vessel punctures) or futile biopsy attempts during the live procedure.

Regarding the IASLC station groupings, because both the aorta and PA lie closer to the left lung than to the right lung, feasible routes were found at a lower rate for *left-lung lymph nodes* (stations 4L and 10L/11L) than for the right lung nodes (4R, 7, and 10R/11R): 6/10 nodes versus 19/21 nodes. In addition, station 7 nodes can be accessed from either the left or right main bronchi, and the station 10R/11R nodes can be accessed through either the right or left upper-lobe bronchi. These observations for our lymph-node test set corroborate a recent multi-center study's findings that physicians biopsied nearly 2× more station 4R nodes than 4L nodes and 35% more 10R/11R nodes than 10L/11L nodes; i.e., physicians biopsied substantially fewer left-lung nodes [9].

3D chest model computation entails roughly 20 min total time, as done in our numerous other image-guided bronchoscopy studies (e.g. Refs. [22,39,40]). In particular, for a typical 250 MB chest CT scan, the automatic operations for 3D chest model computation take ≈15 min total time (airway-tree segmentation, centerline computation, etc.), while semi-automatic lymph-node definition requires ≈1–2 min per node. Given this base computation, route planning is not especially burdensome with a mean computation time = 77 s per Table 2. This computation, which ranged widely from 2.8 s to nearly 5 min per node, however, is hard to predict, as it depends on airway width (larger airways admit more possible poses), node airway depth, accessibility of the node from either/both the left/right sides of the chest, and a node's proximity to occluding vessels.

We next conducted a parameter sensitivity test for safety FOV angle φ_{FOV} in (13). Note that nearly all method parameters are constants determined by the EBUS bronchoscope and associated standard 20-mm-length needle — φ_{FOV} is the only parameter that can be adjusted. For the test, we varied φ_{FOV} from 10° to 50°.

As φ_{FOV} increases, the safety cone becomes wider. This gives a more conservative safety zone but also makes it harder to find an optimal route, as it requires an optimal pose $\mathbf{p}_o$ further from major vessels. Thus, when φ_{FOV} increased from 10° to 50°, the number of nodes yielding a feasible route decreased monotonically from 28/31 to 8/31; no feasible route was found ever for 3/31 lymph nodes (e.g., Fig. 7). More specifically, 23 nodes produced routes for $\varphi_{FOV} \leq 30°$ as shown in Table 5, while 22 nodes produced routes for $\varphi_{FOV} \leq 35°$, 16 nodes for $\varphi_{FOV} \leq 40°$, and 8 nodes over the entire [10°, 50°] range. The nodes in this last 8-node group, which varied substantially in size (9.8 mm $\leq$ long axis $\leq$ 31.8 mm), were in effect "easy" to biopsy safely. To support this observation, 7/8 nodes were located in stations 4R, 10R, or 7 — away from the left side of the chest, which contains the heart and major occluding vasculature. As a result, the mean adequacy values, Γ_o and $\Gamma_{\max}$, were always larger for this subset than for the other nodes over all considered φ_{FOV} values.

A wider safety cone also tends to increase the distance d_{P} to the nodal surface, which decreases the tissue sample size and adequacy. In fact, for the 23-node group, when φ_{FOV} increased from 10° to 30°, mean Γ_o decreased monotonically from 0.49 to 0.41. (Note that the optimal route can change as the optimization parameters change!)

Fig. 8 highlights how sample-size information affords superior visualization of potential biopsy sites. Previous image-guided bronchoscopy work, which did not consider device/needle geometry, lymph-node 3D shape, and nearby occluding vessels, only gives CT-based virtual bronchoscopy (VB) views depicting rudimentary node location, with no indication of advantageous (and disadvantageous) biopsy sites (Fig. 8(b)) [18–22]. In fact, all visible nodal points are projected with equal brightness onto the presented view. Such a view can be extremely misleading, as all visible surface points are depicted, *regardless of their distance from the bronchoscope tip.*

Conversely, our optimal sample size method, which accounts for all factors, clearly indicates the most promising needle puncture sites while also showing obstacles to avoid (Fig. 8(c)). Also, only nodal surface points that enable needle puncture appear — surface points too far from the bronchoscope tip (i.e, have $D(\mathbf{s}_N, \mathbf{n}_N, l_N) = 0.0$) are not displayed. The changing brightness clearly reflects the potential tissue sample size at each visible airway-wall site. Because we know the EBUS bronchoscope's joint video camera and EBUS probe configuration, we can also vividly illustrate how the EBUS probe's FOV (and needle) are situated at

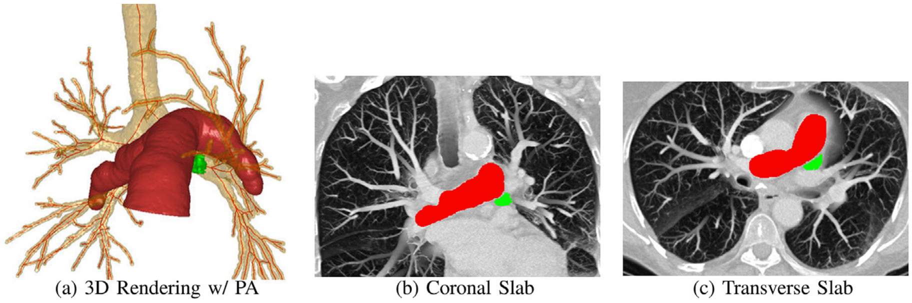

(a) 3D Rendering w/ PA (b) Coronal Slab (c) Transverse Slab

Fig. 7. Station 11L lymph node for patient 5 that did not yield a feasible route. Surface rendering (a) shows how the PA (red) "shields" the lymph node (green) from safe biopsy. Coronal (x–z) and transverse (x–y) sliding thin-slab views (b–c) focused on the PA (red) and lymph node (green) shows how the vessel acts as an obstacle blocking the way to a safe biopsy (depth-weighted maximum views starting at y = 275 for (b) and z = 279 for (c) with depth = 30) [38].

suboptimal poses and also at the optimal pose $\mathbf{p}_o$, as shown in Fig. 8(c) and Section III-B examples.

3.2. Image-guided EBUS bronchoscopy

We have integrated our methodology into a system for image-guided EBUS-TBNA of the central-chest lymph nodes, as discussed more fully in companion papers [41,42]. During the live procedure, the guidance system provides a variety of visualization aids to help the physician maneuver the EBUS bronchoscope along the optimal route of each target lymph node.

Fig. 9 gives an example from navigation to final localization for an enlarged PET-avid station 10L node for patient 10 (PET = positron emission tomography). A chest radiologist identified the node in both the requisite high-resolution chest CT scan and a complementary PET/CT study. The chest CT was produced by a Siemens Sensation-40 scanner, with axial-plane resolution $\Delta x = \Delta y =$ 0.81 mm, section thickness $\Delta z =$ 0.5 mm, and volume dimensions = 512×512×671. The PET/CT study was collected with Philips TrueFlight integrated scanner (PET scan details: $\Delta x = \Delta y =$ 4 mm, $\Delta z =$ 3 mm, volume dimensions = 144×144×312). For the defined node, the CT-based volume = 3.0 cm^3 with principal axes R_a = 30.8 mm, R_b = 14.7 mm, and R_c = 16.4 mm, while PET-based volume = 3.4 cm^3, $\mathrm{SUV}_{\min}$ = 2.7 , $\mathrm{SUV}_{\max}$ = 7.3 , and $\mathrm{SUV}_{\mathrm{mean}}$ = 4.6.

To produce the procedure plan, we fused the PET scan with the chest CT, as discussed in Cheirsilp et al. [43], and then performed CT-based optimal route planning, per the methodology discussed earlier. As the physician navigates the device toward the target node, sample size information is computed in real time and dynamically displayed in a CT-based virtual panorama (Fig. 9(a–c)). As discussed in Zang et al. [42], the virtual panorama expands the FOV of the standard VB view (e.g., Fig. 8(b-c)), which image-guided bronchoscopy systems use to mimic the real videobronchoscope's FOV [17–19]. Taking into account the EBUS bronchoscope's known geometry for the two integrated devices (Fig. 1), the virtual panorama's expanded FOV is now able to present the EBUS probe's FOV in addition to giving a fuller view of nearby occluding vessels. In this way, the virtual panorama greatly helps the physician in deciding where to invoke the EBUS probe and perform the desired biopsy.

Table 5

Sensitivity of adequacy metrics, Γ_o and $\Gamma_{\max}$, to variations in φ_{FOV} for the 23 test lymph nodes giving feasible optimal routes over the angular range [10°, 30°]. Metric values are given as mean±sd and [min, max] range over all 23 nodes.

φ_{FOV}	Γ_o	$\Gamma_{\max}$
10°	49 ± .21 [.15, .93]	63 ± .22 [.23, .95]
15°	47 ± .22 [.09, .93]	63 ± .24 [.13, .95]
20°	44 ± .24 [.05, .93]	57 ± .28 [.08, .95]
25°	43 ± .25 [.04, .93]	56 ± .29 [.05, .95]
30°	41 ± .25 [.02, .93]	54 ± .29 [.04, .95]

Fig. 9(a–c) show that as the EBUS bronchoscope is navigated closer to the lymph node, the node appears progressively "hotter" (more brighter green points appear). Fig. 9(a) illustrates the initial guidance view presented at the beginning of navigation, 42 mm from the target node. Because the EBUS probe has a scan range of 40 mm, the EBUS is out of range of the node and, hence, its fan-shaped FOV icon does not yet appear in the view presented by the guidance system. Furthermore, with the biopsy needle modeled as having a length = 20 mm, no sample size information yet appears. (The arrow of the virtual panorama indicates the direction to navigate the device toward the optimal pose.)

When the device navigates to within 20 mm of the node (Fig. 9(b)), sample size information begins to appear—albeit weakly, indicating the node's location and also the biopsy potential of currently visible sites. In addition, the EBUS transducer's FOV now appears (always top center in compliance with the EBUS bronchoscope's geometry), as do obstacles (red vessels). Notably, the EBUS FOV does not yet observe (i.e., impinge upon) any locations associated with the target node. Thus, at this point of the procedure, the device is both too far from target node, as indicated by the weak sample size display, and not rotated into correct

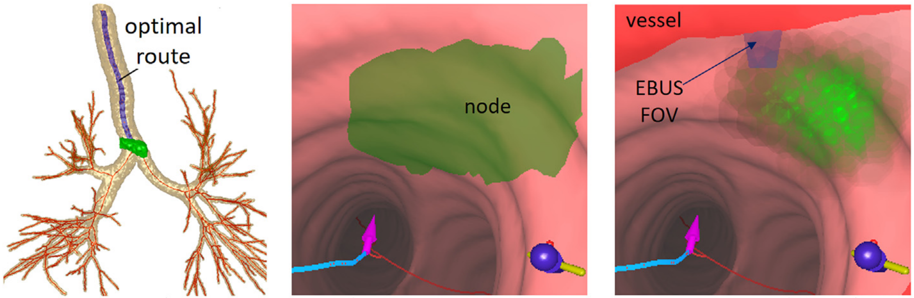

(a) optimal route (b) VB view (previous) (c) VB view with sample size

Fig. 8. Improved nodal visualization for EBUS-guided bronchoscopy along the optimal route derived for a station 4R lymph node of patient 1. (a) 3D CT-based airway-tree rendering (light brown) depicting the optimal route (blue) to the lymph node (green); arrow represents the final pose $\mathbf{p}_o$. (b) Previous node visualization (green) color-blended into CT-based VB view at a view site approaching the optimal pose [22]. (c) Enhanced VB view showing sample size information (green), obstacles (red), and EBUS probe FOV (blue) at the same view site as (b). In this figure and others to follow, the fan-shaped EBUS probe's FOV appears in varying shades of blue and white at maximal sample size locations.

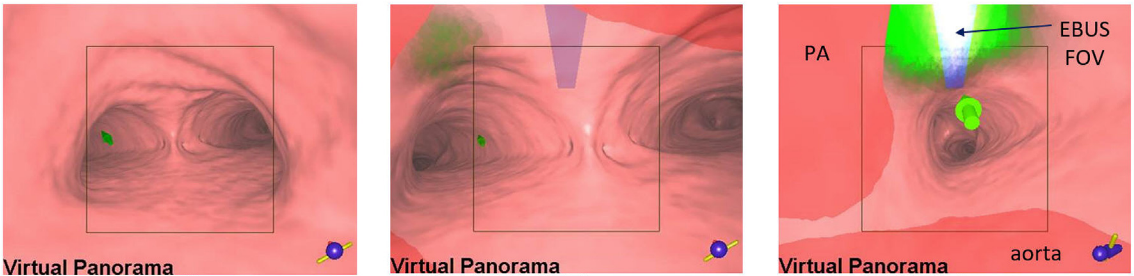

(a) 42 mm (b) 20 mm (c) 8 mm

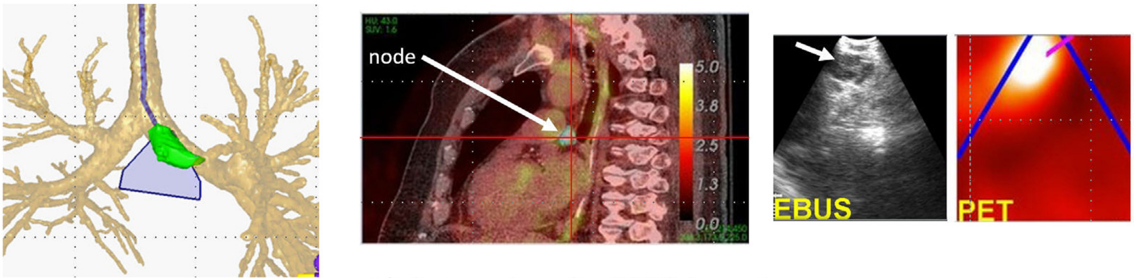

(d) System view after EBUS invocation

Fig. 9. Illustration of tissue sample size visualization and image-guided EBUS bronchoscopy for a station 10L lymph node for patient 10. Parts (a–c) depict the CT-based virtual panorama view after guidance to various sites along the optimal route, where the given measure indicates the bronchoscope's distance to the lymph node's surface. Green-colored locations on a visible airway wall give a visual indication of the biopsy sample size achievable at the given pose, red locations signify occluding vessels, the blue fan shape indicates the EBUS transducer, and the black square signifies with VB view's FOV which also corresponds to the video bronchoscope's FOV (e.g., Fig. 7). Part (c) is located near the final pose $\mathbf{p}_o$ along the optimal route, with the green arrow indicating the optimal sampling direction. Note how the fan-shaped EBUS FOV appears in varying shades of blue in (b–c) as the device gets closer to the optimal pose and becomes white at maximal biopsy sample size locations. Part (d) gives a composite guidance system view after EBUS invocation at the final pose, with all views synchronized to display information at the current pose. Left: The brown surface-rendered airway tree, with the optimal route (blue), EBUS FOV (blue fan shape), and target node (green). Middle: sagittal section of the patient's fused CT-PET volume indicating the target node (left scale is PET SUV). Right: EBUS view of node and corresponding PET-based virtual EBUS at registered site.

position to facilitate a successful biopsy. (Note that the needle's entry port lies within the EBUS probe's scan plane.)

Lastly, Fig. 9(c) shows a view near the optimal pose $\mathbf{p}_o$. For this EBUS bronchoscope pose, the virtual panorama vividly shows the relationships between the large-sample airway-wall locations, EBUS FOV, and occluding vasculature. In particular, the view strongly shows how the EBUS FOV maximizes its overlap at the lymph node's largest feasible tissue sample site, while also facilitating safe biopsy far from the nearby vessels. The preponderance of bright green airway-wall sites clearly signify that the physician has reached the most promising biopsy locations. As corroborating evidence, the EBUS FOV's "white hot" appearance indicates that it now overlaps the airway-wall region having greatest biopsy potential.

After pushing the EBUS probe against the airway wall near $\mathbf{p}_o$, the system composite display of Fig. 9(d) results. The rendered airway tree depicts the optimal airway route and the EBUS FOV's relation to the target lymph node. The fused sagittal CT-PET section confirms the node's location and shows the surrounding major vasculature, while the live EBUS section clearly captures the target node. A segmentation of this nodal view using the method of Zang et al. gives major and minor axes equal to 11.8 mm and 5.5 mm, respectively [39]. Note that the precomputed metrics at $\mathbf{p}_o$ had values $\Gamma_o = 11.9$ mm, $\Gamma_{\max} = 17.1$ mm, $\alpha_o = 0.60$, and $\alpha_{\max} = 0.86$. (Based on the CT's resolution, we believe these measures to be reliable to within ± 1.5 mm) Thus, the nodal segmentation supports the notion that the biopsy needle at this location would yield a good tissue sample and roughly pierce a length comparable to the derived Γ_o and $\Gamma_{\max}$. Finally, the PET-based view in Fig. 9(d) adds still more confirmation on the importance of biopsying this PET-avid node at the indicated location, as it represents a PET-based "virtual EBUS" view found by registering the fused CT/PET-based virtual space to the live EBUS view's "real" 3D coordinate system [42].

In general, during an image-guided procedure, the device's current pose $\mathbf{p}$ is always known. Hence, the sample size calculations (10), (13), and (17–18) need only be performed for the small set of airway-wall sites observed by the virtual bronchoscope's FOV at $\mathbf{p}$. In addition, an associated alpha-blending surface-rendering algorithm combines the sample size information, CT-based airway-wall surfaces, nodes, and vessels to display all structures simultaneously. All sample size and display calculations are done in parallel and computed using the GPU of the guidance computer's video card.

Overall, we have performed a progressive series of phantom and patient studies to help establish system functionality, safety, and feasibility in a live clinical environment [41,44,45]. A companion paper gives a full discussion of the guidance system and our most recent human studies [42].

4. Discussion

Given that nearly 200,000 patients undergo lung-cancer staging each year in the United States, it is vital that EBUS TBNA's general effectiveness be improved [46]. This need is amplified by the ongoing roll-out of CT-based lung-cancer screening, which is increasing the patient population requiring staging and also demanding the biopsy of smaller nodes, presumably more difficult to sample effectively [47]. In addition, reliable bronchoscopic methods for adequate tissue sampling are being called upon for evidence-based lung-cancer treatment planning, lung precision medicine, and the search for airway biomarkers aiding early lung-cancer detection/monitoring [48–50].

Unfortunately, skill variations in interpreting patient chest CT scans and in using EBUS limit staging effectiveness [11]. In particular, the accuracy of localizing target lymph nodes and the selection of safe, effective biopsy sites is inadequate, as it involves manual trial-and-error methods.

We have presented an automatic procedure planning method for

EBUS bronchoscopy. Our method adds four innovations to previous efforts. First, optimal tissue sample size information indicates the most effective biopsy sites for maximizing the tissue acquired during EBUS-TBNA biopsy. Second, the geometry of occluding vessels is accounted for to enable safe obstacle avoidance. Third, the geometric specifications of the multimodal EBUS bronchoscope are incorporated to facilitate later image-guided bronchoscopy. Fourth, as the physician maneuvers the EBUS bronchoscope through the airways during the live procedure, dynamic sample size visualization cues appear in real time to clearly indicate the most effective EBUS TBNA biopsy sites while also pointing out unsafe locations to avoid.

Overall, the method provides a *physician-independent* method for understanding nodal biopsy potential and quality *before* a procedure and intuitive dynamic feedback on effective biopsy sites *during* a procedure. The physician is able to discern whether a biopsy may be “easy” or overly risky. In addition, the method offers flexibility in adjusting safety margins. Furthermore, the pre-procedure computation is not burdensome, while the guidance feedback occurs in real-time during bronchoscopy. Finally, the method is easily adaptable to other devices, such as the experimental 5.9-mm distal-end diameter EBUS bronchoscope recently put forth by Olympus [51]. Also, we have begun to adapt our method to the critical complementary problem of EBUS TBNA-based tissue sampling of peripheral nodules for lung-cancer diagnosis, which draws upon radial-probe EBUS [52,53].

Our quantitative results indicate that the method potentially enables successful biopsies in essentially 100% of selected lymph nodes versus the 70–94% success rate of other studies. The method also potentially facilitates maximal tissue samples giving adequate tissue biopsies for nearly 100% of selected nodes, as opposed to the 55–77% tissue adequacy rates of standard methods. We caution, however, that our results depend on the choice of human cases and lymph nodes; cases were selected without bias, as they arose, however. Nevertheless, larger studies would help better understand true efficacy.

Several clinical issues warrant mention. First, to increase the likelihood of collecting an adequate tissue sample, physicians generally make several passes at a given node, with the reported mean number of needle passes per node ranging from 2.0 to 4.6 [7,9,54]. In addition, needle size (21 gauge versus 22 gauge), the availability of rapid on-site evaluation (ROSE), and the use of PET imaging can affect TBNA effectiveness and the number of passes made. Unfortunately, the diagnostic yield for lymph node staging — i.e., the ability to make a specific disease diagnosis for the patient based on bronchoscopic nodal sampling — only ranges from 37% to 51%, as reported in various multi-center studies and meta-analysis [8,9,55].

A major factor here is that physicians sample too few nodes during staging. In fact, separate multi-center studies by Ost and Yarmus reported that physicians sampled only 2.04 and 2.3 lymph nodes per patient, respectively [8,9]. Despite some belief that EBUS TBNA's safety profile is acceptable, physicians have shown reluctance in biopsying “harder” sites [48]. Also, needle passes can be inadequate and it has been put forth that the physician must sample the “right” part of a node to find the disease. With the increasing prevalence of CT screening for early cancer detection, it will be vital for physicians to follow the stated guideline of *comprehensive nodal staging,* whereby many nodal stations spanning the chest must be sampled to reach a proper diagnosis [56]. This requires that the physician have a method that instills greater confidence in nodal sampling, facilitates faster biopsy (so more nodes can be biopsied), and enables more accurate tissue sampling, independent of physician skill. Our proposed methodology could help meet these requirements, and we have been striving to incorporate the method into a protocol for image-guided comprehensive nodal staging [57].

Acknowledgments

This work was partially supported by grant R01-CA151433 from the National Cancer Institute of the NIH. William E. Higgins and Penn State have an identified conflict of interest and financial interest related to this research. These interests have been reviewed by the University's Institutional and Individual Conflict of Interest Committees and are currently being managed by the University and reported to the NIH.

References

[1] R.L. Siegel, K.D. Miller, A. Jemal, Cancer statistics, CA A Cancer J. Clin. 65 (2015) 5–29 Jan.-Feb. 2015.
[2] A.D. Sihoe, A.P. Yim, Lung cancer staging, J. Surg. Res. 117 (Mar. 2004) 92–106.
[3] G. Silvestri, A. Gonzalez, M. Jantz, M. Margolis, et al., Methods for staging non-small cell lung cancer: diagnosis and management of lung cancer, third ed., American College of Chest Physicians Evidence-Based Clinical Practice Guidelines,” Chest, vol. 143, May 2013, pp. e211S–e250S.
[4] F. Sheski, P. Mathur, Endobronchial ultrasound, Chest 133 (Jan. 2008) 264–270.
[5] M.M. Wahidi, F.J.F. Herth, A. Ernst, State of the art: interventional pulmonology, Chest 131 (Jan. 2007) 261–274.
[6] K.P. Wang, A.C. Mehta, J.F. Turner Jr., Flexible Bronchoscopy, third ed., John Wiley & Sons, 2012.
[7] G. Hong, J. Koo, Evaluation of the gauge of needles used in the collection of specimens during endobronchial ultrasound-guided transbronchial needle aspiration, J. Bras. Pneumol. 45 (Jan.-Feb. 2019) e20180090.
[8] D.E. Ost, A. Ernst, X. Lei, D. Feller-Kopman, et al., Diagnostic yield of endobronchial ultrasound-guided transbronchial needle aspiration: results of the AQuIRE bronchoscopy registry, Chest 140 (Dec. 2011) 1557–1566.
[9] L. Yarmus, J. Akulian, N. Lechtzin, F. Yasin, D. Feller-Kopman, et al., Comparison of 21-gauge and 22-gauge aspiration needle in endobronchial ultrasound-guided transbronchial needle aspiration: results of the american college of chest physicians quality improvement registry, education, and evaluation registry, Chest 143 (April 2013) 1036–1043.
[10] T. Panchabhai, A. Mehta, Historical perspectives of bronchoscopy: connecting the dots, Annals Am. Thorac. Soc. 12 (May 2015) 631–641.
[11] M. Wahidi, C. Hulett, N. Pastis, G. Silvestri, et al., Learning experience of linear endobronchial ultrasound among pulmonary trainees, Chest 145 (March 2014) 574–578.
[12] K. Hopper, T. Lucas, K. Gleeson, J. Stauffer, R. Bascom, D. Mauger, R. Mahraj, Transbronchial biopsy with virtual CT bronchoscopy and nodal highlighting, Radiology 221 (Nov. 2001) 531–536.
[13] M. Betancourt, L. Marron, R. Khare, W. Higgins, R. Bascom, Simulation of mediastinal node site selection: comparison of transverse CT scans and virtual navigation system guidance, Am. J. Respir. Crit. Care Med. 179 (April 2009) A6149.
[14] H.P. McAdams, P.C. Goodman, P. Kussin, Virtual bronchoscopy for directing transbronchial needle aspiration of hilar and mediastinal lymph nodes: a pilot study, Am. J. Roentgenol. 170 (May 1998) 1361–1364.
[15] H. Minami, Y. Ando, F. Nomura, S. Sakai, K. Shimokata, Interbronchoscopist variability in the diagnosis of lung cancer by flexible bronchoscopy, Chest 105 (June 1994) 1658–1662.
[16] S.A. Merritt, J.D. Gibbs, K.C. Yu, V. Patel, L. Rai, D.C. Cornish, R. Bascom, W.E. Higgins, Real-time image-guided bronchoscopy for peripheral lung lesions: a phantom study, Chest 134 (Nov. 2008) 1017–1026.
[17] P. Reynisson, H. Leira, T. Hernes, E. Hofstad, et al., Navigated bronchoscopy: a technical review, J. Bronchology Interv. Pulmonol. 21 (July 2014) 242–264.
[18] F.J. Herth, R. Eberhardt, M. Schuhmann, Bronchoscopy in lung cancer: navigational modalities and their clinical use, Expert Rev. Respir. Med. 10 (Aug. 2016) 901–906.
[19] F. Asano, Practical application of virtual bronchoscopic navigation, in: A. Mehta, P. Jain (Eds.), Interventional Bronchoscopy, vol. 10, Humana Press, 2013, pp. 121–140 Respir. Med..
[20] R. Eberhardt, N. Kahn, D. Gompelmann, M. Schumann, C.P. Heussel, F.J. Herth, “LungPoint — a new approach to peripheral lesions, J. Thorac. Oncol. 5 (Oct. 2010) 1559–1563.
[21] S. Merritt, R. Khare, R. Bascom, W. Higgins, Interactive CT-video registration for image-guided bronchoscopy, IEEE Trans. Med. Imaging 32 (Aug. 2013) 1376–1396.
[22] J. Gibbs, M.W. Graham, R. Bascom, D. Cornish, R. Khare, W. Higgins, Optimal procedure planning and guidance system for peripheral bronchoscopy, IEEE Trans. Biomed. Eng. 61 (March 2014) 638–657.
[23] X. Luo, K. Mori, Beyond current guided bronchoscopy: a robust and real-time bronchoscopic ultrasound navigation system, in: K. Mori, I. Sakuma, Y. Sato, C. Barillot, N. Navab (Eds.), MICCAI 2013, Springer, Sep. 2013, pp. 388–395 *Lecture Notes in Computer Science* **8149**.
[24] M. Sato, F. Chen, A. Aoyama, T. Yamada, M. Ikeda, T. Bando, H. Date, Virtual endobronchial ultrasound for transbronchial needle aspiration, J. Thorac. Cardiovasc. Surg. 146 (Nov. 2013) 1204–1212.
[25] H. Sorger, E. Hofstad, T. Amundsen, T. Lango, J. Bakeng, H. Leira, A multimodal image guiding system for navigated ultrasound bronchoscopy (EBUS): a human feasibility study, PLoS One 12 (2) (9 Feb. 2017) e0171841.
[26] M.W. Graham, J.D. Gibbs, D.C. Cornish, W.E. Higgins, Robust 3D airway-tree segmentation for image-guided peripheral bronchoscopy, IEEE Trans. Med. Imaging 29 (Apr. 2010) 982–997.
[27] J.D. Gibbs, M.W. Graham, W.E. Higgins, 3D MDCT-based system for planning peripheral bronchoscopic procedures, Comput. Biol. Med. 39 (Mar. 2009) 266–279.
[28] K.C. Yu, E.L. Ritman, W.E. Higgins, System for the analysis and visualization of large 3D anatomical trees, Comput. Biol. Med. 37 (Dec. 2007) 1802–1820.

[29] P. Taeprasartsit, W.E. Higgins, Robust extraction of the aorta and pulmonary artery from 3D MDCT images, 7623, in: B. Dawant, D. Haynor (Eds.), SPIE Medical Imaging 2010: Image Processing, 2010 76230H–1—76230H–17.

[30] P. Taeprasartsit, W.E. Higgins, Robust method for extracting the pulmonary vascular trees from 3D MDCT images, SPIE Medical Imaging 2011: Image Processing, 2011 796237–1—796237–17.

[31] K. Lu, W.E. Higgins, Interactive segmentation based on the live wire for 3D CT chest image analysis, Int. J. Computer Assisted Radiol. Surgery 2 (Dec. 2007) 151–167.

[32] K. Lu, W.E. Higgins, Segmentation of the central-chest lymph nodes in 3D MDCT images, Comput. Biol. Med. 41 (9) (2011) 780–789.

[33] A.P. Kiraly, J.P. Helferty, E.A. Hoffman, G. McLennan, W.E. Higgins, 3D path planning for virtual bronchoscopy, IEEE Trans. Med. Imaging 23 (Nov. 2004) 1365–1379.

[34] J.A. Hartigan, M.A. Wong, A k-means clustering algorithm, Applied Statistics 28 (1979) 100–108.

[35] X. Zang, EBUS/MDCT Fusion For Image-Guided Bronchoscopy, PhD thesis The Pennsylvania State University, Department of Computer Science and Engineering, 2016.

[36] I.T. Joliffe, Principal Component Analysis, second ed., Springer, 2002.

[37] A. El-Sherief, C. Lau, C. Wu, R. Drake, G. Abbott, T. Rice, International association for the study of lung cancer (IASLC) lymph node map: radiologic review with CT illustration, RadioGraphics 34 (Oct. 2014) 1680–1691.

[38] J.Z. Turlington, W.E. Higgins, New techniques for efficient sliding thin-slab volume visualization, IEEE Trans. Med. Imaging 20 (Aug. 2001) 823–835.

[39] X. Zang, R. Bascom, C. Gilbert, J. Toth, W. Higgins, Methods for 2-D and 3-D endobronchial ultrasound image segmentation, IEEE Trans. Biomed. Eng. 63 (July 2016) 1426–1439.

[40] R. Khare, R. Bascom, W. Higgins, Hands-free system for bronchoscopy planning and guidance, IEEE Trans. Biomed. Eng. 62 (Dec. 2015) 2794–2811.

[41] W. Higgins, X. Zang, R. Cheirsilp, P. Byrnes, T. Kuhlengel, J. Toth, R. Bascom, Optimal multimodal virtual bronchoscopy for convex-probe endobronchial ultrasound, 10576, in: B. Fei, R. Webster (Eds.), SPIE Medical Imaging 2018: Image-Guided Procedures, Robotic Interventions, and Modeling, 2018 1057618–1 — 1057618–6.

[42] X. Zang, R. Cheirsilp, P. Byrnes, T. Kuhlengel, T. Allen, R. Mahraj, C. Abendroth, J. Toth, R. Bascom, and W. Higgins, “System for image-guided ebus bronchoscopy,” Int. J. Comput. Assist. Radiol. Surgery , in preparation 2019.

[43] R. Cheirsilp, R. Bascom, T. Allen, R. Mahraj, W.E. Higgins, Deformable image registration for multimodal lung-cancer staging, 9784, in: M. Styner, E. Angelini (Eds.), SPIE Medical Imaging 2016: Image Processing, 2016 9784Z–1 — 9784Z–10.

[44] W.E. Higgins, X. Zang, R. Cheirsilp, P. Byrnes, T. Kuhlengel, J. Toth, R. Bascom, System for multimodal image-guided endobronchial ultrasound: human pilot study, Am. J. Respir. Crit. Care Med. 193 (May 2016) A4382.

[45] W.E. Higgins, X. Zang, P. Byrnes, T. Kuhlengel, R. Cheirsilp, J. Toth, R. Bascom, Optimal biopsy-site localization for image-guided endobronchial ultrasound, Am. J. Respir. Crit. Care Med. 195 (May 2017) A2873.

[46] G.A. Silvestri, A.V. Gonzalez, F.C. Detterbeck, et al., Methods for staging non-small cell lung cancer: diagnosis and management of lung cancer: American College of Chest Physicians evidence-based clinical practice guidelines, Chest 143 (May 2013) e211S–e250S.

[47] L.T. Tanoue, N.T. Tanner, M.K. Gould, G.A. Silvestri, Lung cancer screening, Am. J. Respir. Crit. Care Med. 191 (1 Jan. 2015) 19–33.

[48] E. Folch, D.B. Costa, J. Wright, P.A. VanderLaan, “Lung cancer diagnosis and staging in the minimally invasive age with increasing demands for tissue analysis,” *Transl*, Lung Cancer Res 4 (Aug. 2015) 392–403.

[49] A.C. Wu, J.P. Kiley, P.J. Noel, et al., Current status and future opportunities in lung precision medicine research with a focus on bimarkers, Am. J. Respir. Crit. Care Med. 198 (15 Dec. 2018) 1479–1489.

[50] E. Billatos, J. Vick, M. Lenburg, A. Spira, The airway transcriptome as a biomarker for early lung cancer detection, Clin. Cancer Res. 24 (July 2018) 2984–2992.

[51] P. Patel, H. Wada, H.-P. Hu, K. Hirohashi, K. Yasufuku, et al., First evaluation of the new thin convex probe endobronchial ultrasound scope: a human ex vivo lung study, Ann. Thorac. Surg. 103 (April 2017) 1158–1164.

[52] D.E. Ost, A. Ernst, J. Toth, et al., Diagnostic yield and complications of bronchoscopy for peripheral lung lesions. results of the AQuIRE registry, Am. J. Respir. Crit. Care Med. 193 (1 Jan. 2016) 68–77.

[53] W. Zhao, R. Bascom, J. Toth, W. Higgins, Guidance system development for radial-probe endobronchial ultrasound bronchoscopy, 10951, in: B. Fei, C. Linte (Eds.), SPIE Medical Imaging 2019: Image-Guided Procedures, Robotic Interventions, and Modeling, 2019 109511P–1 — 109511P–7.

[54] J. Saji, N. Kurimoto, K. Morita, M. Nakamura, T. Inoue, H. Nakamura, T. Miyazawa, Comparison of 21-gauge and 22-gauge needles for endobronchial ultrasound-guided transbronchial needle aspiration of mediastinal and hilar lymph nodes, J. Bronchol. Intervent. Pulmonol. 18 (3) (2011) 239–246.

[55] K. Adams, P.L. Shah, L. Edmonds, E. Lim, Test performance of endobronchial ultrasound and transbronchial needle aspiration biopsy for mediastinal staging in patients with lung cancer: systematic review and meta-analysis, Thorax 64 (Sept. 2009) 757–762.

[56] F. Detterbeck, J. Puchalski, A. Rubinowitz, D. Cheng, Classification of the thoroughness of mediastinal staging of lung cancer, Chest 137 (Feb. 2010) 436–442.

[57] T. Kuhlengel, W. Higgins, Bronchoscopic procedure planning for systematic lymph node analysis, 10951, in: B. Fei, C. Linte (Eds.), SPIE Medical Imaging 2019: Image-Guided Procedures, Robotic Interventions, and Modeling, 2019 109511O–1 — 109511O–7.

Rebecca Bascom. received the A.B. degree in French studies from Harvard University, Cambridge, MA, the M.D. degree in medicine from Oregon Health Sciences University, Portland, OR, and the and M.Ph. degrees in occupational health from Johns Hopkins University, Baltimore, MD. She has held positions previously at Johns Hopkins University and the University of Maryland. She is currently a professor of medicine at the Pennsylvania State University Hershey Medical Center. Her research interests are in pulmonary medicine and occupational health.

Patrick Byrnes. received the Ph.D. degree in electrical engineering from The Pennsylvania State University, University Park, PA. He is currently an assistant professor in computer science and software engineering at Penn State Behrend, Erie, PA. His research interests are in the broad areas of computer vision and video analysis.

Ronnarit Cheirsilp. received the Ph.D. degree in computer science and engineering from The Pennsylvania State University, University Park, PA. He is currently employed at Broncus Medical, San Jose, CA. His research interests are in multimodal imaging processing and analysis, computer graphics, and interactive system development.

Jason Gibbs. received the Ph.D. degree in electrical engineering from The Pennsylvania State University, University Park, PA. He was previously employed at Broncus Medical, San Jose, CA. He is currently employed at X-Nav Technologies, Lansdale, PA.

William E. Higgins. received the B.S. degree in electrical engineering from the Massachusetts Institute of Technology, Cambridge, MA, and the M.S. and Ph.D. degrees in electrical engineering from the University of Illinois, Urbana-Champaign. He has held positions previously at the Honeywell Systems and Research Center, Minneapolis, MN, and the Mayo Clinic, Rochester, MN. He is currently a distinguished professor of electrical engineering, computer science and engineering, and bioengineering at the Pennsylvania State University. His research interests are in image-guided intervention systems and in multidimensional medical image processing and visualization.